

CHRISTIAN MICHELSEN
NIELS BOHR INSTITUTE
UNIVERSITY OF COPENHAGEN

A PHYSICIST'S
APPROACH TO
MACHINE LEARNING
—
UNDERSTANDING
THE BASIC BRICKS

SUPERVISOR:
TROELS PETERSEN
NIELS BOHR INSTITUTE
UNIVERSITY OF COPENHAGEN

Copyright © 2019

Christian Michelsen

`HTTPS://GITHUB.COM/CHRISTIANMICHELSEN`

Licensed under the Apache License, Version 2.0 (the “License”); you may not use this file except in compliance with the License. You may obtain a copy of the License at <http://www.apache.org/licenses/LICENSE-2.0>. Unless required by applicable law or agreed to in writing, software distributed under the License is distributed on an “AS IS” BASIS, WITHOUT WARRANTIES OR CONDITIONS OF ANY KIND, either express or implied. See the License for the specific language governing permissions and limitations under the License.

First printing, December 2019

Contents

1	<i>Abstract</i>	1
2	<i>Introduction</i>	3
3	<i>Machine Learning Theory</i>	7
3.1	<i>Statistical Learning Theory</i>	7
3.2	<i>Supervised Learning</i>	8
3.3	<i>Generalization Bound</i>	9
3.3.1	<i>Generalization Bound for infinite hypotheses</i>	11
3.4	<i>Avoiding overfitting</i>	12
3.4.1	<i>Model Regularization</i>	12
3.4.2	<i>Cross Validation</i>	14
3.4.3	<i>Early Stopping</i>	16
3.5	<i>Loss functions</i>	16
3.5.1	<i>Evaluation Function</i>	18
3.6	<i>Decision Trees</i>	18
3.6.1	<i>Ensembles of Decision Trees</i>	19
3.7	<i>Hyperparameter Optimization</i>	21
3.7.1	<i>Grid Search</i>	22
3.7.2	<i>Random Search</i>	22
3.7.3	<i>Bayesian Optimization</i>	23
3.8	<i>Feature Importance</i>	25
4	<i>Danish Housing Prices</i>	29
4.1	<i>Data Preparation and Exploratory Data Analysis</i>	30
4.1.1	<i>Correlations</i>	32
4.1.2	<i>Validity of input variables</i>	33
4.1.3	<i>Cuts</i>	34

4.2	<i>Feature Augmentation</i>	35
4.2.1	<i>Time-Dependent Price Index</i>	36
4.3	<i>Evaluation Function</i>	37
4.4	<i>Initial Hyperparameter Optimization</i>	38
4.5	<i>Hyperparameter Optimization</i>	40
4.6	<i>Results</i>	42
4.7	<i>Model Inspection</i>	45
4.8	<i>Multiple Models</i>	47
4.9	<i>Discussion</i>	49
5	<i>Particle Physics and LEP</i>	55
5.1	<i>The Standard Model</i>	55
5.2	<i>Quark Hadronization</i>	57
5.3	<i>The ALEPH Detector and LEP</i>	58
5.4	<i>Jet clustering</i>	60
5.5	<i>The variables</i>	60
6	<i>Quark Gluon Analysis</i>	65
6.1	<i>Data Preprocessing</i>	65
6.2	<i>Explanatory Data Analysis</i>	66
6.3	<i>Loss and Evaluation Function</i>	69
6.4	<i>b-Tagging Analysis</i>	70
7	<i>Discussion and Outlook</i>	75
8	<i>Conclusion</i>	77
8.1	<i>Tufte-\LaTeX Website</i>	77
8.2	<i>Tufte-\LaTeX Mailing Lists</i>	77
8.3	<i>Getting Help</i>	77
A	<i>Housing Prices Appendix</i>	79
B	<i>Quarks vs. Gluons Appendix</i>	105
	<i>Index</i>	115

List of Figures

3.1	Overview of the learning problem.	8
3.2	Approximation-Estimation tradeoff	12
3.3	Regularization Effect	13
3.4	Regularization Effect of L_2	14
3.5	Regularization Effect of L_1	14
3.6	k -Fold Cross Validation	15
3.7	k -Fold Cross Validation for Time Series Data	15
3.8	Comparison of different objective functions.	18
3.9	Comparison of different objective functions zoom in.	18
3.10	Decision Tree Cuts In Feature Space	18
3.11	Decision Tree	19
3.12	Grid Search	22
3.13	Random Search	23
3.14	Bayesian Optimization	24
4.1	Danish Housing Price Index	29
4.2	Distributions for the housing price dataset	30
4.3	Distributions for the housing price dataset	31
4.4	Histogram of prices of houses and apartments sold in Denmark	32
4.5	Linear correlation between variables and price	33
4.6	MIC non-linear correlation.	33
4.7	Non-linear correlation between variables and price	34
4.8	Validity of input features	34
4.9	Validity Dendrogram	35
4.10	Prophet Forecast for apartments	36
4.11	Prophet Trends	37
4.12	XXX	38
4.13	Overview of initial hyperparameter optimization of the housing model for apartments	39
4.14	XXX	40
4.15	XXX	40
4.16	XXX	41
4.17	Hyperparameter optimization: random search results	42
4.18	Early Stopping results	42
4.19	Performance of XGB-model on apartment prices	43
4.20	2018 XGB Forecast	43
4.21	2018 XGB Forecast	44
4.22	SHAP Prediction Explanation for apartment	46
4.23	Feature importance of apartments prices using XGB	46

4.24 Feature importance of apartments prices using XGB XXX	47
4.25 Multiple Models XXX	48
4.26 SHAP plot villa TFIDF XXX	50
5.1 The Standard Model	56
5.2 Feynman diagram for the jet production at LEP	57
5.3 Quark splitting	57
5.4 Hadronization process	58
5.5 The ALEPH detector	59
5.6 Polar angle	59
5.7 Azimuthal angle	59
6.1 Histograms of the vertex variables	67
6.2 UMAP visualization of vertex variables for 4-jet events	68
6.3 UMAP visualization of vertex variables for 3-jet events	68
6.4 UMAP visualization of vertex variables for 2-jet events	68
6.5 Correlation of Vertex Variables	69
6.6 Plot of the log-loss ℓ_{\log}	70
6.7 b-tag scores in 3-jet events	71
6.8 ROC curve for b-tag in 4-jet events	71
6.9 g-tag scores in 4-jet events	72
6.10 g-tag scores in 4-jet events for signal and background	72
6.11 ROC curve for g-tag in 4-jet events	72
6.12 1D Sum Model Cuts for 4-jets	72
6.13 1D Sum Models Predictions and Signal Fraction for 4-jets	73
6.14 Hyperparameter Optimization of b- and g-tagging	73
6.15 Overview of Hyperparameters of g-tagging for 3-jet shuffled events	73
6.16 SHAP Prediction Explanation for b-like jet	73
6.17 Monte Carlo – Data bias for b-tags and jet energy	74
6.18 b-Tagging Efficiency $\epsilon_b^{b\text{-sig}}$ as a function of jet energy	74
6.19 b-Tagging Efficiency $\epsilon_b^{g\text{-sig}}$ as a function of jet energy	74
6.20 b-Tagging Efficiency $\epsilon_g^{g\text{-sig}}$ as a function of jet energy	74
6.21 b-Tagging Efficiency $\epsilon_g^{b\text{-sig}}$ as a function of jet energy	75
6.22 g-Tagging proxy efficiency for $b\bar{b}g$ -events as function of the mean invariant mass	75
6.23 g-Tagging proxy efficiency for $b\bar{b}g$ -events as function of g-tag	75
6.24 g-Tagging efficiency for 4-jet events in MC as a function of normalized gluon gluon jet energy difference	75
6.25 Closure plot between MC Truth and the corrected g-tagging model in 4-jet events for the normalized gluon gluon jet energy difference	76
6.26 R kt CA overview XXX TODO!	76
6.27 R kt CA cut region A XXX TODO!	76
A.1 Validity Heatmap	79
A.2 Distributions for the housing price dataset	80
A.3 Distributions for the housing price dataset	81
A.4 Distributions for the housing price dataset	82
A.5 Distributions for the housing price dataset	83
A.6 Distributions for the housing price dataset	84

A.7 Distributions for the housing price dataset	85
A.8 Distributions for the housing price dataset	86
A.9 Distributions for the housing price dataset	87
A.10 Distributions for the housing price dataset	88
A.11 Distributions for the housing price dataset	89
A.12 Distributions for the housing price dataset	90
A.13 Distributions for the housing price dataset	91
A.14 Distributions for the housing price dataset	92
A.15 Distributions for the housing price dataset	93
A.16 Linear Correlations	95
A.17 MIC non-linear correlation	96
A.18 Prophet Forecast for apartments	96
A.19 Prophet Trends	96
A.20 Overview of initial hyperparameter optimization of the housing model for houses	100
A.21 XXX	101
A.22 XXX	101
A.23 XXX	101
A.24 XXX	102
A.25 XXX	102
A.26 XXX	102
A.27 Performance of XGB-model on apartment prices	103
B.1 UMAP Parameter Grid Search	106
B.2 Visualization of the t-SNE algorithm	106

List of Tables

4.1	XXX TODO! .	31
4.2	XXX TODO! .	35
4.3	XXX TODO! .	35
4.4	XXX TODO! .	35
4.5	XXX TODO! .	35
4.6	train test split XXX TODO! .	38
4.7	train test split tight XXX TODO! .	38
4.8	Cauchy-ejerlejlighed.	39
4.9	Cauchy-villa.	39
4.10	XXX	41
4.11	XXX	43
4.12	XXX ejer	45
4.13	XXX villa	45
6.1	The dimensions of the dataset for the actual Data. The numbers in the jet columns are the number of events multiplied with the number of jets; e.g. $85 \cdot 6 = 510$.	66
6.2	The dimensions for the MC and MCb datasets.	66
6.3	Number of different types of jets for MC and MCb. See also Table B.1 in the appendix for relative numbers.	67
A.1	XXX TODO! .	94
A.2	Rmse-ejerlejlighed-appendix.	97
A.3	Logcosh-ejerlejlighed-appendix.	97
A.4	Cauchy-ejerlejlighed-appendix.	97
A.5	Welsch-ejerlejlighed-appendix.	98
A.6	Fair-ejerlejlighed-appendix.	98
A.7	Rmse-villa-appendix.	98
A.8	Logcosh-villa-appendix.	98
A.9	Cauchy-villa-appendix.	99
A.10	Welsch-villa-appendix.	99
A.11	Fair-villa-appendix.	99
A.12	XXX ejer tight	104
A.13	XXX villa tight	104
B.1	Number of different types of jets for MC and MCb written in relative numbers such that each row sum to 100 %. See also Table 6.3.	105

1. Abstract

Here will be a decent abstract at some point™.

Part I

The first part of this thesis deals with the introductory theory of machine learning and its predictive power in estimating Danish housing prices.

Part II

The second part of this thesis deals with particle physics and the discriminatory power of machine learning for quark-gluon identification and subsequent analysis.

6. Quark Gluon Analysis

AS ANY DEDICATED READER can clearly see, the Ideal of practical reason is a representation of, as far as I know, the things in themselves; as I have shown elsewhere, the phenomena should only be used as a canon for our understanding. The paralogsms of practical reason are what first give rise to the architectonic of practical reason. As will easily be shown in the next section, reason would thereby be made to contradict, in view of these considerations, the Ideal of practical reason, yet the manifold depends on the phenomena.

6.1 Data Preprocessing

The data consists of 43 data files taken between 1991 and 1995 totalling 3.5 GB (Data). Along with this comes 125 files based on Monte Carlo (MC) simulations (8.4 GB) and additional 42 MC-files with only b -quark events (MCb) simulated (2.1 GB). The data files which are in the form of *Ntuples*, ROOT's data format [25], are converted to HDF5-files by using uproot [6]. While iterating over the *Ntuples*, some basic cuts are applied before exporting the data to HDF5. The first one being that the (center of mass) energy E in the event has to be within $90.8 \text{ GeV} \leq E \leq 91.6 \text{ GeV}$ to only use the Z peak data. The second one being that the sum of the momenta p_{sum} in each event is $32 \text{ GeV} \leq p_{\text{sum}}$ to remove any $Z \rightarrow \tau^+ \tau^-$ events. To ensure a primary vertex, at least two good tracks are required where a good track is defined as having 7 TPC hits and ≥ 1 silicon hit. Finally it is required that the cosine of the thrust axis polar angle, which is the angle between the thrust axis and the beam, is less than or equal to 0.8 to avoid any low angle events since the detector performance worsens significantly in that region. These cuts were standard requirements for the ALEPH experiment.

One last cut which was experimented with was the threshold value for *jet matching*. The jet matching is the process of matching the jet with one of the final state quarks. The jet is said to be matched if the dot product of between the final quark momentum and the jet momentum is more than then threshold value. Higher thresholds means cleaner jets but at the expense of less statistics. A jet matching threshold of 0.90 was found to be a good compromise between purity and quantity where 97.8 % of all 2-jet events are

matched and 96.7% of all other jets were matched¹.

The data structure is quite differently structured in the Ntuples compared to normal structured data in the form of tidy data [73]. The data is organized such that one iterates over each event where the variables are variable-length depending on the number of jets in the events; this is also known as *jagged* arrays. The data is un-jagged² before exporting to HDF5-format and only the needed variables are kept. This reduces the total output file to a 2.9 GB HDF5-file for both Data, MC, and MCb.

The number of events for each number of jets can be seen in Table 6.1 for the Data and in Figure 6.2 for the MC and MCb.

6.2 Explanatory Data Analysis

Since the machine learning models are only trained on the three vertex variables `projet`, `bqvjet`, and `ptljet` – see chapter 5 for a deeper introduction to these variables – these variables will be the primary focus of this section. Given the fact that MC-simulated data exists, the truth of each simulated event is also known. This allows us visualize the difference between the different types of quarks. In the MC simulation each event are generated such that the type of quark, or *flavor*, is known and assigned the variable `flevt`. The mapping from flavor to `flevt` is:

Flavor:	<i>bb</i>	<i>cc</i>	<i>ss</i>	<i>dd</i>	<i>uu</i>
<code>flevt</code> :	5	4	3	2	1

In addition to knowing the correct flavor, we define that an event is *q-matched* if one, and only one, of the jets are assigned to one of the quarks, one, and only one, of the jets are assigned to the other quark, and no other jets are matched to any of the quarks. We can then define what constitutes a *b-jet*: if it has `flevt` = 5, the entire event is *q-matched*, and the jet is matched to one of the quarks. Similarly we define *c-jets* only with the change that `flevt` = 5, and *uds-jets* with `flevt` ∈ {1,2,3}. A gluon jet is defined as an any-flavor event which is *q-matched* but the jet is not assigned to any of the quarks. Strictly speaking, this means that *g-jet* is not 100% certain of being a gluon, however, since the MC simulation does not contain this information this is the only option. Due to the *q-match* criterion this also means that some jets are assigned the label “non-*q-matched*” which is regarded as background. The distribution of different types of jets can be seen in Table 6.3 and shown as relative numbers in Table B.1 in the appendix.

With the criteria defined above for what constitutes a specific type of jet the 1D-distributions for the three vertex variables is plotted in Figure 6.1. For all three subplots the histograms are shown with a logarithmic *y*-axis, all *b-jets* in blue, *c-jets* in red, *g-jets* in green and all jets in orange. In fully opaque color are shown the distributions for 2-jet events, in dashed (and lighter color) 3-jet

¹ Compare this to 98.5% and 97.8% for a threshold of 0.85 or 95.9% and 93.9% for a threshold of 0.95.

² Such that e.g. a 3-jet event will figure as three rows in the dataset.

	jets	events
2	2 359 738	1 179 869
3	3 619 290	1 206 430
4	854 336	213 584
5	52 775	10 555
6	510	85
Total	6 886 649	2 610 523

Table 6.1: The dimensions of the dataset for the actual Data. The numbers in the jet columns are the number of events multiplied with the number of jets; e.g. $85 \cdot 6 = 510$.

	jets	events
2	7 293 594	3 646 797
3	10 780 890	3 593 630
4	2 241 908	560 477
5	103 820	20 764
6	588	98
Total	20 420 800	7 821 766

Table 6.2: The dimensions for the MC and MCb datasets.

	<i>b</i>	<i>c</i>	<i>uds</i>	<i>g</i>	non- <i>q</i> -matched
2	2 713 454	944 380	2 125 900	0	1 509 860
3	2 433 878	964 212	2 129 218	3 365 969	1 887 613
4	326 264	156 332	336 548	1 012 198	410 566
5	10 332	5960	12 668	54 525	20 335
6	42	26	52	320	148
Total	5 483 970	2 070 910	4 433 012	4 604 386	3 828 522

events, and in semi-transparent 4-jet events. In the left subplot the `projet` variable is plotted where it can be seen that high values of `projet` tend to indicate *b*-jets. In the middle subplot `bqvjet` is plotted which shares many similarities with the `projet`-variables, including that high values indicate *b*-jets. In the right subplot the `ptljjet` is plotted. This variable has many zeros in it which correlates with mostly with gluon³ and large values are mostly due to *b*-jets. In general it is clear to see how the differences in distribution between the 2-, 3-, and 4-jet events are minor, with the one exception of 2-jet events which does not contain any gluons at all.

Table 6.3: Number of different types of jets for MC and MCb. See also Table B.1 in the appendix for relative numbers.

³ Around 98 % of all *g*-jets are zeros compared to $\sim 82\%$ for *c*-jets and $\sim 70\%$ for *b*-jets.

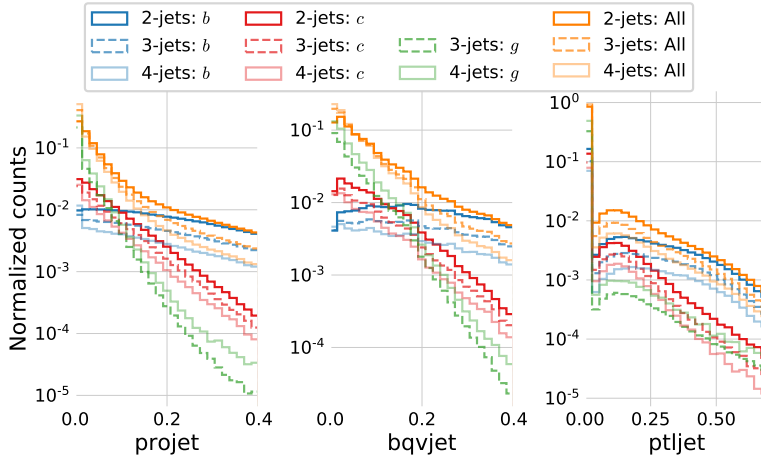


Figure 6.1: Normalized histograms of the three vertex variables: `projet`, `bqvjet`, and `ptljjet`. In blue colors the variables are shown for *blue b-jets*, in red for *true c-jets*, in green for *true g-jets*, and in orange for *all of the jets* (including non *q*-matched). In fully opaque color are shown the distributions for 2-jet events, in dashed (and lighter color) 3-jet events, and in semi-transparent 4-jet events. Notice the logarithmic y-axis, that there are no *g*-jets for 2-jet events (as expected), and that all of the distributions are very similar not matter how many jets.

Even though there are only three vertex variables, it is difficult to properly get an intuition about how easily separated they different types of jets are. Since there are millions of points a single 3D scatter plot quickly becomes overcrowded in one wants to plot all jets. We apply dimensionality reduction from the three dimensions down to two dimensions by using the UMAP algorithm [48]. Within recent years the field of dimensionality reduction algorithms has grown a lot from just the typical (linear) principal component analysis to also include non-linear algorithms. The t-SNE algorithm [67] deserves an honorable mention since this algorithm revolutionized the usage of (nonlinear) dimensionality reduction algorithms in e.g. bioinformatics [65, 71] yet its mathematical foundation has strongly been improved with the never, faster UMAP algorithm [48] which usage is also expanding [18, 19, 31].

The aim of UMAP, short for Uniform Manifold Approximation and Projection, is to correctly identify and preserve the structure, or topology, of the high-dimensional feature space in a lower-dimensional output space. It does so by trying to stitch together local manifolds in the high-dimensional feature space such that the difference between the high- and low-dimensional representations is minimized according to the cross-entropy such that both global structure and local structure is preserved [48]. Compared to t-SNE the approach in UMAP has an algebraic topological background compared to the more heuristic approach taken by t-SNE. Note that the UMAP algorithm is not provided any information about which jets are which types.

The UMAP algorithm has several hyperparameters, where two of the most important ones are the number of neighbors `n_neighbors` which controls the priority between correctly preserving the global versus the local structure, and the `min_dist` which defines how tightly together UMAP is allowed to cluster the points in the low-dimensional representation. To properly choose the best combination of `n_neighbors` and `min_dist` a grid search with `n_neighbors` $\in \{10, 50, 100, 250\}$ and `min_dist` $\in \{0, 0.2, 0.5\}$ is performed. This is shown for 4-jet events in Figure B.1 in the appendix. In this case the choice of best combination of `n_neighbors` and `min_dist` is subjective at best, but it was judged by the author that `n_neighbors` = 250 and `min_dist` 0.2 gave the best compromise between preserving local and global structure. The results of running UMAP on 4-jet events can be seen in Figure 6.4. Here the millions of points are plotted using Datashader [7] to avoid overplotting and colored according to the jet type. From the figure it is seen how there are some clear, blue *b*-jet clusters, however, most of the data seem to be a mix of *g*- and *uds*-jets. The plots with the same UMAP parameters for 3-jet and 2-jet events are seen in Figure 6.3 and 6.4.

These figures suggests that it should be possible to discriminate the *b*-jets from the other jets somewhat, however, no clear separation is expected. The t-SNE algorithm was also tested but showed inferior performance compared to UMAP, see Figure B.2 in the appendix for an example of this.

The correlation between the vertex variables can be seen in Figure 6.5, where the upper diagonal shows the linear correlation ρ and the lower diagonal shows the (estimate of the) MIC non-linear correlation MIC_e . Here it can be seen that `projet` and `bqvjet` correlate mostly whereas the other variables correlate a lot less. Had they all correlated a lot, it would be more difficult to extract any meaningful insights from the system as it would contain less information.

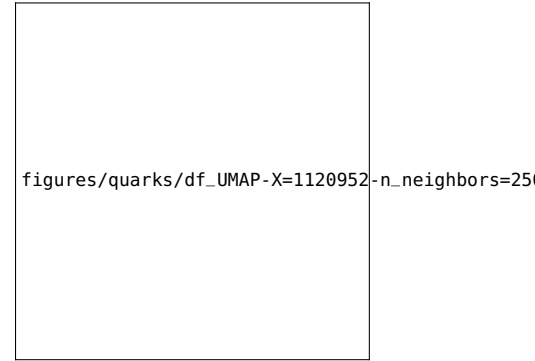


Figure 6.2: Visualization of the vertex variables for the different categories: `true b-jets` in blue, `true c-jets` in red, `true uds-jets` in green, `true g-jets` in orange, and `non q-matched` events in purple. The clustering is performed with the UMAP algorithm which outputs a 2D-projection. This projection is then visualized using the Datashader which takes care of point size, avoids over and underplotting, and color intensity.

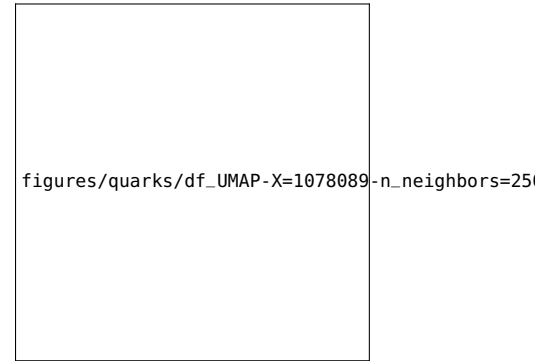


Figure 6.3: UMAP visualization of vertex variables for 3-jet events.

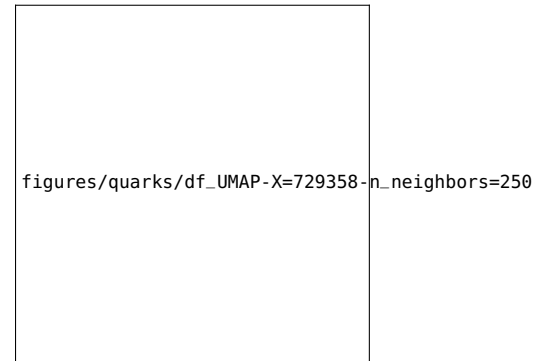


Figure 6.4: UMAP visualization of vertex variables for 2-jet events.

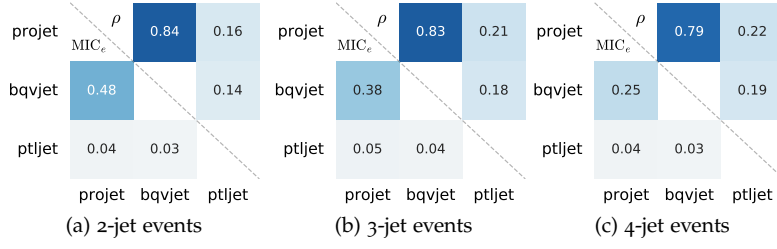


Figure 6.5: Correlation of the three vertex variables for 2-, 3- and 4-jet events.

6.3 Loss and Evaluation Function

In contrary to the housing prices subproject the goal in this project is to predict the class of particles, or the types of jets, where the so-called *signal* observations⁴ are often assigned the label 1 and *background* observations 0. The combination of this being a *classification* problem (compared to a regression problem) along with the fact all the variables are actual measurements from a particle physics accelerator means that the issue of outliers is negligible. This also means that the problem of finding a robust loss function is non-existent since the in classification loss is already bounded in the $[0, 1]$ -interval.

Classically *accuracy* is often used as loss function for classification which is simply the fraction of correct predictions, however, accuracy as a metric suffers a lot when handling *imbalanced* data: when the ratio between the number of instances of each class is not approximately (50 : 50)%. The problem is that if the sample contains 90 % background and only 10 % signal, then a simple model which simply predicts everything to be background will have a 90 % accuracy.

To circumvent this issue, the area under the ROC curve (AUC) is used, where the ROC⁵ curve is the the *signal efficiency* ε_{sig} of the ML model plotted as a function of the *background efficiency* ε_{bkg} . The definition of these two measures are:

$$\varepsilon_{\text{sig}} = \frac{S_{\text{sel}}}{S_{\text{tot}}}, \quad \varepsilon_{\text{bkg}} = \frac{B_{\text{sel}}}{B_{\text{tot}}}, \quad (6.1)$$

where S_{sel} are signal events that were also selected (predicted) as signal by the ML model, $S_{\text{tot}} = S_{\text{sel}} + S_{\text{rej}}$ is the total number of signal events (the selected and rejected), and likewise for background events B . Within the machine learning community the signal efficiency is called the true positive rate (TPR) and the background efficiency the false positive rate (FPR). For the rest of this project, the AUC will be the evaluation function, however, since this metric does not work on single observations it cannot be used as the loss function. Instead we will use the *log-loss* as the loss function⁶ which not only is differentiable for single predictions, compared to AUC, but also takes the certainty of the prediction into account. When using tree-based algorithms or neural networks one can extract not only whether or not a single observation is classified as signal or background but also a prediction score. This is a number in the $[0, 1]$ -interval and the closer to 1 the score is, the more certain

⁴ Often called *signal events*, however, this term would require that each event constitutes a single data point in the dataset which it does not here.

⁵ Receiver Operating Characteristic.

⁶ In the context of machine learning this is the same as the *cross entropy*.

the model is of the prediction being signal. Given the prediction score \hat{y} and the true label y , the log-loss ℓ_{\log} is calculated as:

$$\ell_{\log} = -y \log \hat{y} - (1 - y) \log (1 - \hat{y}). \quad (6.2)$$

This is visualized in Figure 6.6. Here it can be seen how the loss changes as a function of the prediction score. Notice that when $y = 0$ the loss is undefined for $\hat{y} = 1$ and likewise with $y = 1$ and $\hat{y} = 0$ (since $\log 0$ is undefined).

6.4 *b*-Tagging Analysis

The ability to discriminate between the different types of particles produced in a collision is obviously import to understand the results. Today much work go into tagging algorithms from *b*-tagging in ATLAS and CMS [58] but this work started even decades ago. That *b*-quarks are tagged specifically is both due to *b*-quarks having more unique characteristics compared to e.g. *c*-quarks and are thus easier to tag, but also the fact that *b*-quarks are the second-heaviest of the quarks and are measured to better understand CP⁷-violation at LHC-b, contributes to the choice of tagging *b*-quarks. In ALEPH Proriot et al. [53] started the work of comparing different methods for *b*-tagging already in 1991. They concluded that a neural network had the best performance compared to e.g. a linear (Fisher) discriminant. The neural network used was a 3-layer neural network (NN) trained on nine variables and the output `nmbjet`. For this of this project this pre-trained network will be called NNB.

The data are split⁸ into training and test sets in such a way that the individual jets in an event are not split. As such, the splitting is performed at event-scale in a (80 : 20)% train-test ratio.

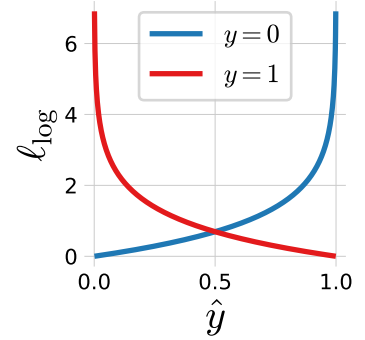


Figure 6.6: Plot of the log-loss ℓ_{\log} .

⁷ Short for charge-parity.

⁸ After removing all low-energy jets such that all events that contain any jets with an energy of less than 4 GeV are removed.

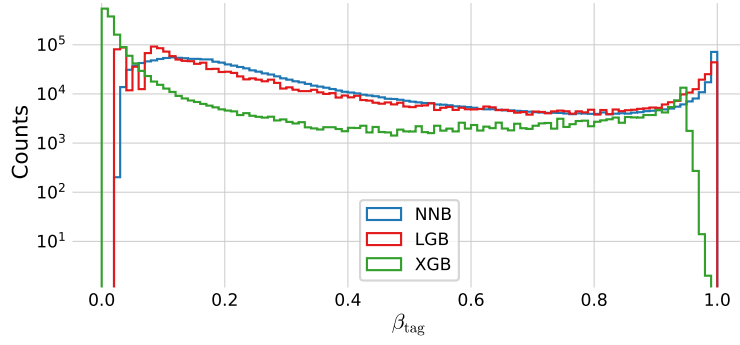


Figure 6.7: Histogram of b-tag scores (model prediction) in 3-jet events for **NNB** (the neural network trained by ATLAS, also called `nbnjet`) in blue, **XGB** in red, and **XGB** in green. We see that the XGB predictions closely match those of NNB which is a good confirmation of a successful fit.

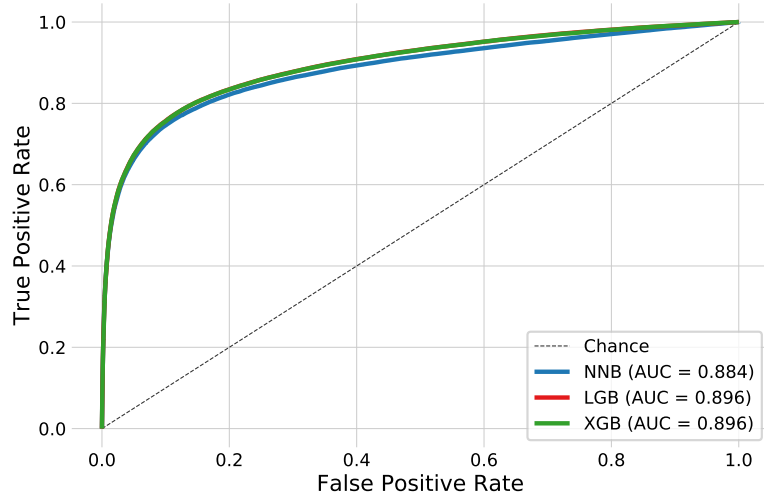


Figure 6.8: ROC curve of the three b-tag models in 3-jet events for **NNB** (the neural network trained by ATLAS, also called `nbnjet`) in blue, **XGB** in red, and **XGB** in green. In the legend the Area Under Curve (AUC) is also shown. Notice that the XGB and XGB models share performance and it is thus due to overplotting that only the green line for XGB can be seen. In the particle physics community False Positive Rate (FPR) is sometimes better known as background efficiency and True Positive Rate (TPR) as signal efficiency.

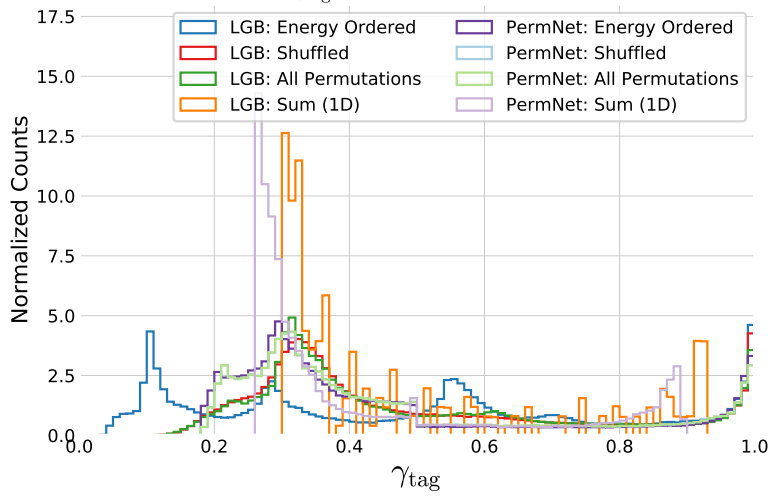


Figure 6.9: Histogram of g-tag scores (model prediction) in 4-jet events for XGB: Energy Ordered in blue, XGB: Shuffled in red, XGB: All Permutations in green, XGB: Sum 1D in orange, PermNet: Energy Ordered in purple, PermNet: Shuffled in light-blue, PermNet: All Permutations in light-green, PermNet: Sum 1D in light-purple. Here XGB and PermNet are the two different type of models and “Energy Ordered”, “Shuffled”, “All Permutations”, and “Sum 1D” are the different methods used for making the input data permutation invariant.

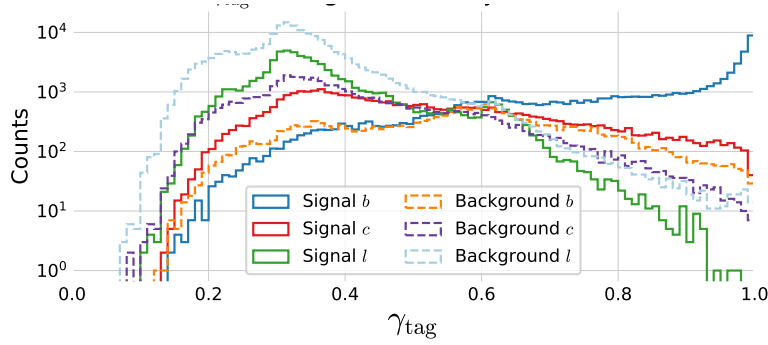


Figure 6.10: Histogram of g-tag scores (model prediction) from the XGB-model in 4-jet events for b signal in blue, c signal in red, l signal in green, b background in orange, c background in purple, l background in light-blue.

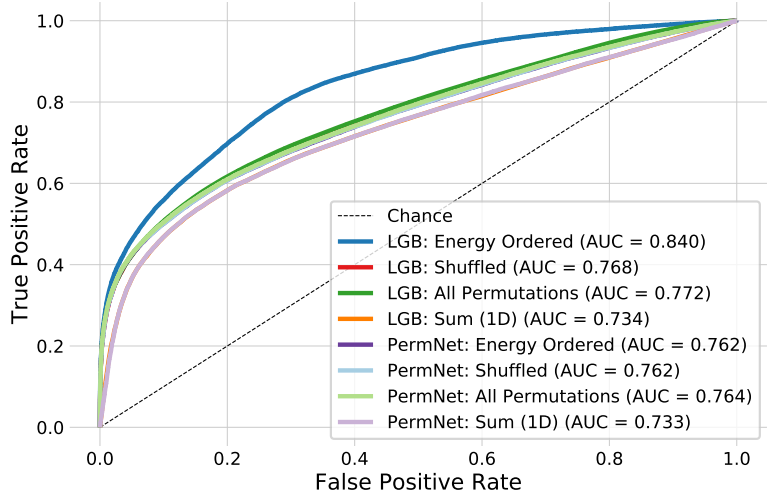


Figure 6.11: ROC curve of the eight g-tag models in 4-jet events. First one in dashed black is the ROC curve that you get by random chance. The colors are the same as in Figure 6.9 and in the legend also the Area Under the ROC curve (AUC) is shown. Notice that the XGB model which uses the energy ordered data produced the best model, however, this model is not permutation invariant. Of the permutation invariant models (the rest), the XGB model trained on all permutations of the b-tags performs highest. The lowest performing models are the two models trained only on the 1-dimensional sum of b-tags, as expected, however, still with a better performance than expected by the author.

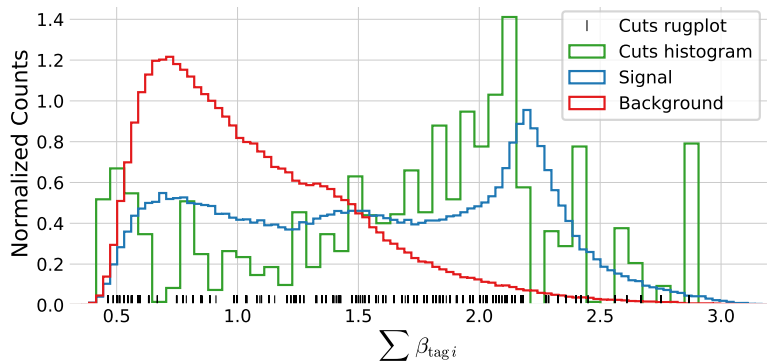


Figure 6.12: Histogram of the distribution of signal in blue and background in red for 1-dimensional sum of b-tags training data. A histogram of the cut values from the XGB model trained on this data is shown in green together with a rug plot of the cut values in black. Notice how most of the cuts match up with the signal peak at around a $\sum \beta_i \sim 2.1$, however, there are also quite a lot of cuts around $\sum \beta_i \sim 0.5$.

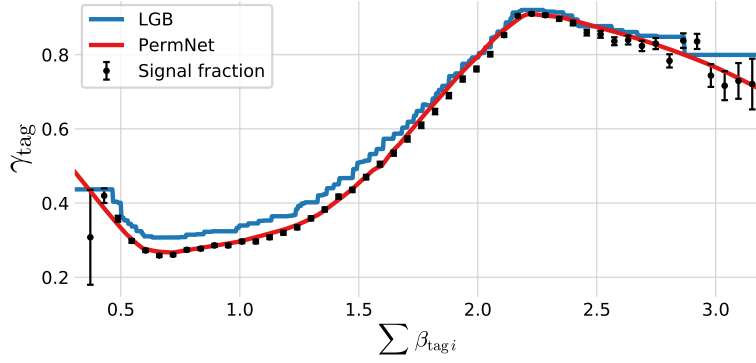


Figure 6.13: Plot of the (1D) g-tag scores as a function of $\sum \beta_i$ for the XGB model in blue and the PermNet model in red. Here the g-tag scores are just the models' output values when input a uniformly spaced grid of $\sum \beta_i$ values between 0 and 4. The signal fraction (based on the signal and background histograms in Figure 6.12) is plotted as black error bars where the size of the error bars is based on the propagated uncertainties of the signal and background histogram assuming Poissonian statistics. Notice how both models capture the overall trend of the signal fraction with the PermNet being particularly close.

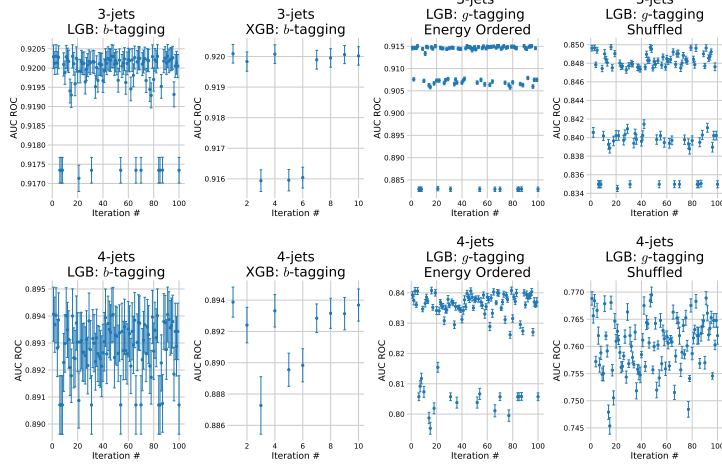


Figure 6.14: Hyperparameter Optimization (HPO) results after running 100 iterations of Random Search (only 10 for XGB). In the top row are the results of the 3-jet models and in the bottom row the results of the 4-jet models. From left to right, we have first) the b-tagging results of XGB, second) the b-tagging results of XGB using only 10 iterations of RS, third) the g-tagging results of XGB fit on the Energy Ordered b-tags, and forth) the g-tagging results of XGB fit on the shuffled b-tags. Notice the different ranges on the y-axes.

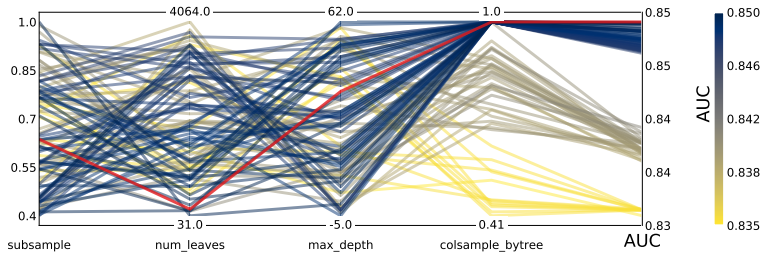


Figure 6.15: Hyperparameter optimization results of g-tagging for 3-jet shuffled events. The results are shown as parallel coordinates with each hyperparameter along the x-axis and the value of that parameter on the y-axis. Each line is an event in the 4-dimensional space colored according to the performance of that hyperparameter as measured by AUC from highest AUC in dark blue to lowest AUC in yellow. The single best hyperparameter is shown in red.

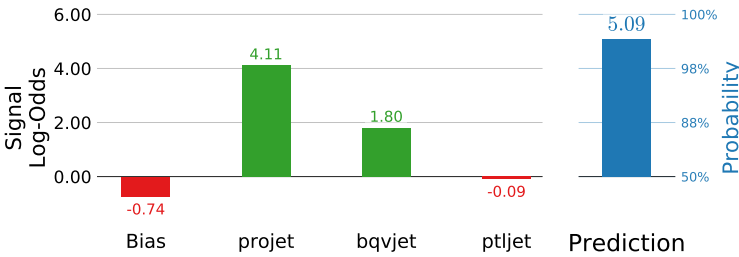


Figure 6.16: Model explanation for the 3-jet b-tagging model for a b-like jet. The first column is the bias of the training set which acts as the naive prediction baseline, the rest are the input data variables. On the right hand side of the plot is the model prediction shown. The left part of the plot is shown in log-odds space, the right part in probability space. The model prediction is the sum of the log-odds (5.09 in this example) transformed into probability space. The negative log-odd values are shown in red, positive ones in green, and the prediction value in blue.

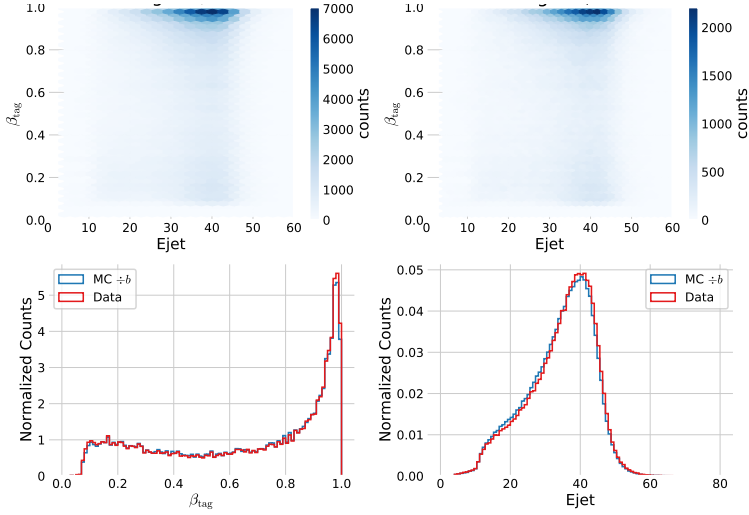


Figure 6.17: Comparison of the b-tag and jet energy (E_{jet}) distributions for Monte Carlo (MC) versus data. In the top row the 2D-distributions are shown for MC on the left (without the extra MCb samples) and data on the right. In the bottom row the 1D marginal distributions are shown for the b-tag and the jet energy with **data** in red and **Monte Carlo** ones in blue. Notice the the almost identical distributions in b-tag.

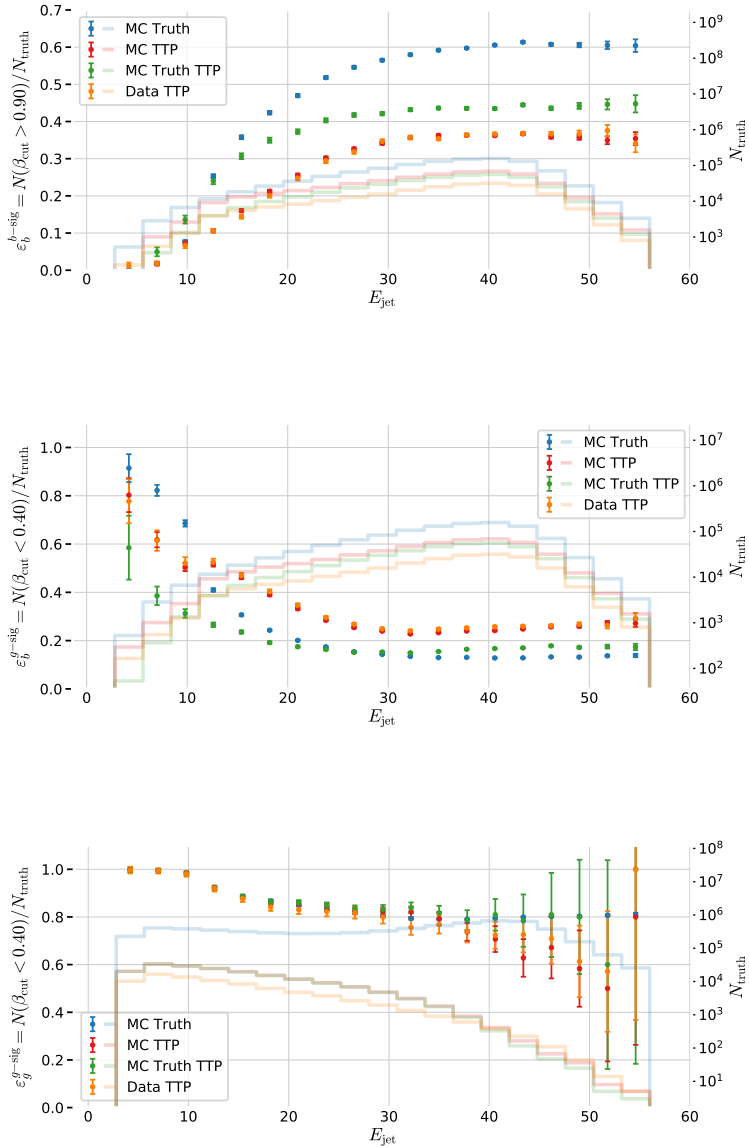


Figure 6.18: Efficiency of the b-tags for b-jets in the b-signal region for 3-jet events, $\epsilon_b^{b\text{-sig}}$, as a function of jet energy E_{jet} . The b-signal region is defined as $\beta > 0.9$. In the plot the efficiencies are shown for **MC Truth** in blue, **MC TTP** in red, **MC Truth TTP** in green, and **Data TTP** in orange. The efficiencies (the errorbars) can be read off on the left y-axis and the counts (histograms) on the right y-axis. The abbreviation TTP is short for “Tag, Tag, Probe” where two jets in a event are used as tags and the probe is then used for further analysis. Notice how both MC TTP and Data TTP follow each other closely.

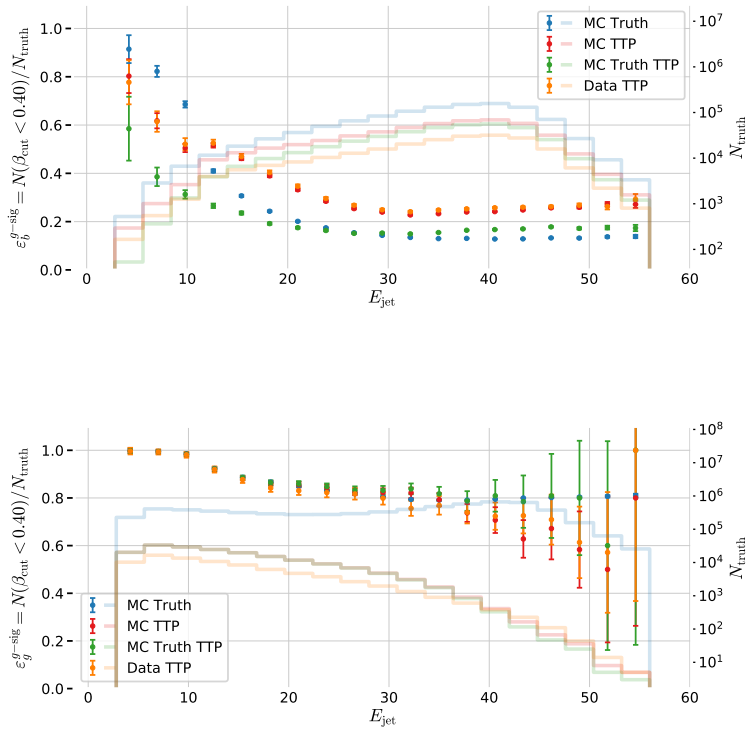


Figure 6.19: Efficiency of the b-tags for g-jets in the g-signal region for 3-jet events, $\epsilon_g^{g\text{-sig}}$, as a function of jet energy E_{jet} . The g-signal region is defined as $\beta < 0.4$. In the plot the efficiencies are shown for **MC Truth** in blue, **MC TTP** in red, **MC Truth TTP** in green, and **Data TTP** in orange. The efficiencies (the errorbars) can be read off on the left y-axis and the counts (histograms) on the right y-axis. The abbreviation TTP is short for “Tag, Tag, Probe” where two jets in a event are used as tags and the probe is then used for further analysis. Notice how both MC TTP and Data TTP follow each other closely.

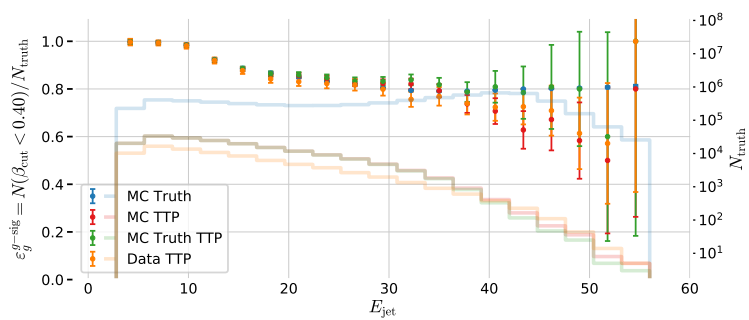


Figure 6.20: Efficiency of the b-tags for g-jets in the g-signal region for 3-jet events, $\epsilon_g^{g\text{-sig}}$, as a function of jet energy E_{jet} . The g-signal region is defined as $\beta < 0.4$. In the plot the efficiencies are shown for **MC Truth** in blue, **MC TTP** in red, **MC Truth TTP** in green, and **Data TTP** in orange. The efficiencies (the errorbars) can be read off on the left y-axis and the counts (histograms) on the right y-axis. The abbreviation TTP is short for “Tag, Tag, Probe” where two jets in a event are used as tags and the probe is then used for further analysis. Notice how both MC TTP and Data TTP follow each other closely.

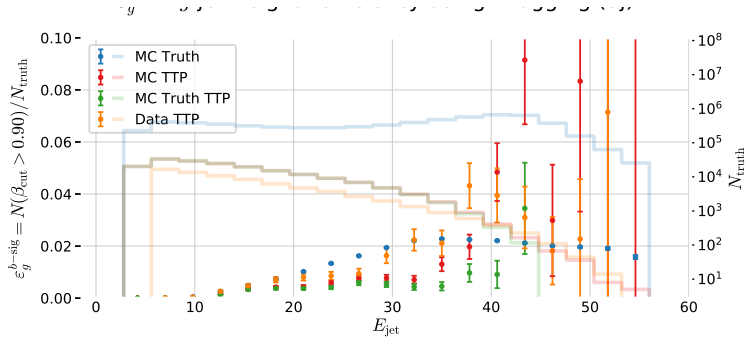


Figure 6.21: Efficiency of the b-tags for g-jets in the b-signal region for 3-jet events, $\epsilon_g^{b\text{-sig}}$, as a function of jet energy E_{jet} . The b-signal region is defined as $\beta > 0.9$. In the plot the efficiencies are shown for **MC Truth** in blue, **MC TTP** in red, **MC Truth TTP** in green, and **Data TTP** in orange. The efficiencies (the errorbars) can be read off on the left y-axis and the counts (histograms) on the right y-axis. The abbreviation TTP is short for “Tag, Tag, Probe” where two jets in a event are used as tags and the probe is then used for further analysis.

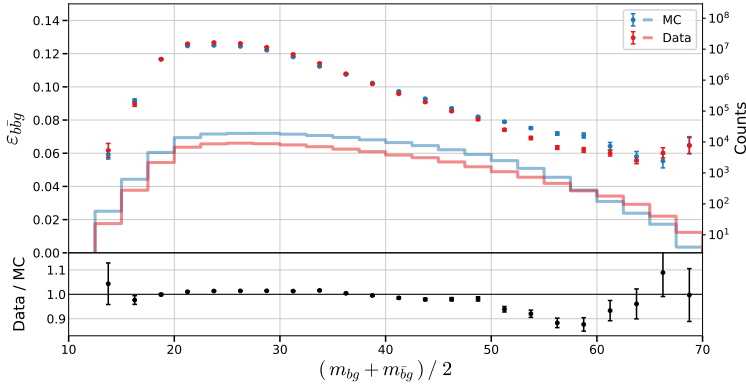


Figure 6.22: Proxy efficiency of the g-tags for $b\bar{b}g$ 3-jet events as a function of the mean of the two invariant masses m_{bg} and $m_{b\bar{g}}$. The proxy efficiency ϵ_{bbg} is measured by finding $b\bar{b}g$ -events where $\beta_b > 0.9$, $\beta_{\bar{b}} > 0.9$, and $\beta_g < 0.4$, and then calculating $\epsilon_{bbg} = \epsilon_b^{b\text{-sig}} \cdot \epsilon_{\bar{b}}^{b\text{-sig}} \cdot \epsilon_g^{g\text{-sig}}$. In the top plot ϵ_{bbg} is shown for **MC** in blue and **Data** in red where the counts in each bin can be read on right y-axis. In the bottom plot the ratio between Data and MC is shown.

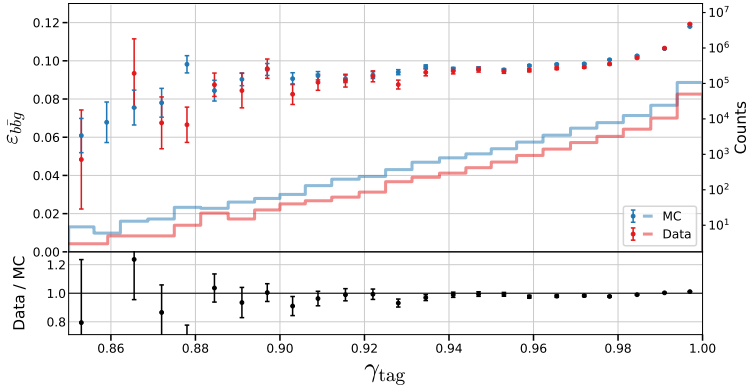


Figure 6.23: Proxy efficiency of the g-tags for $b\bar{b}g$ 3-jet events as a function of the event’s g-tag. The proxy efficiency ϵ_{bbg} is measured by finding $b\bar{b}g$ -events where $\beta_b > 0.9$, $\beta_{\bar{b}} > 0.9$, and $\beta_g < 0.4$, and then calculating $\epsilon_{bbg} = \epsilon_b^{b\text{-sig}} \cdot \epsilon_{\bar{b}}^{b\text{-sig}} \cdot \epsilon_g^{g\text{-sig}}$. In the top plot ϵ_{bbg} is shown for **MC** in blue and **Data** in red where the counts in each bin can be read on right y-axis. In the bottom plot the ratio between Data and MC is shown.

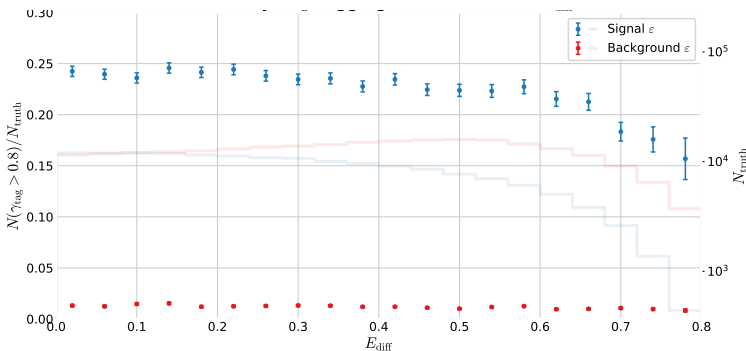


Figure 6.24: Efficiency of the g-tags for 4-jet events as a function of normalized gluon gluon jet energy difference in Monte Carlo. The efficiency is measured as the number of events with a g-tag higher than 0.8 ($\gamma > 0.8$) out of the total number and the normalized gluon gluon jet energy difference A is $A = \frac{E_{g\text{max}} - E_{g\text{min}}}{E_{g\text{max}} + E_{g\text{min}}}$ where $E_{g\text{max}}$ ($E_{g\text{min}}$) refers to the energy of the gluon with the highest (lowest) energy. The efficiency is plotted for **signal events** according to MC Truth in blue and **background events** according to MC Truth in red.

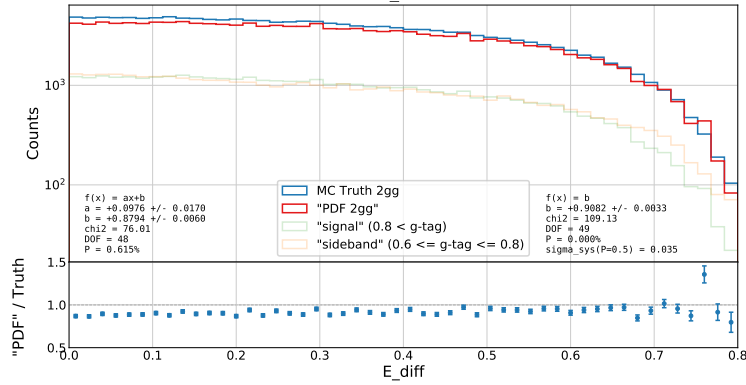


Figure 6.25: Closure plot between MC Truth and the corrected g-tagging model in 4-jet events for the normalized gluon gluon jet energy difference. The corrected g-tagging model is described in further detail in section XXX **TODO!**. In the top part of the plot the MC Truth is shown in blue, the corrected g-tagging model "PDF 2gg" in red, the g-signal distribution in semi-transparent green and the g-sideband distribution in semi-transparent orange. In the bottom part of the plot the ratio between MC Truth and the output of the corrected g-tagging model is shown. The normalized gluon gluon jet energy difference A is $A = \frac{E_{gmax} - E_{gmin}}{E_{gmax} + E_{gmin}}$ where E_{gmax} (E_{gmin}) refers to the energy of the gluon with the highest (lowest) energy.

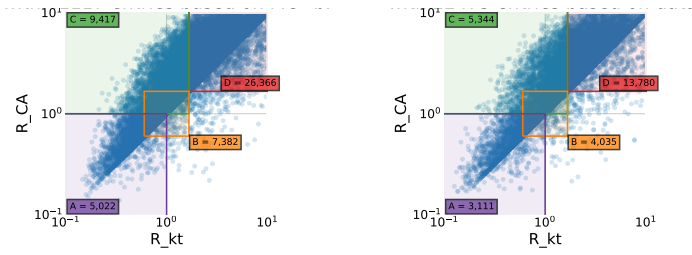


Figure 6.26: R kt CA overview XXX **TODO!**

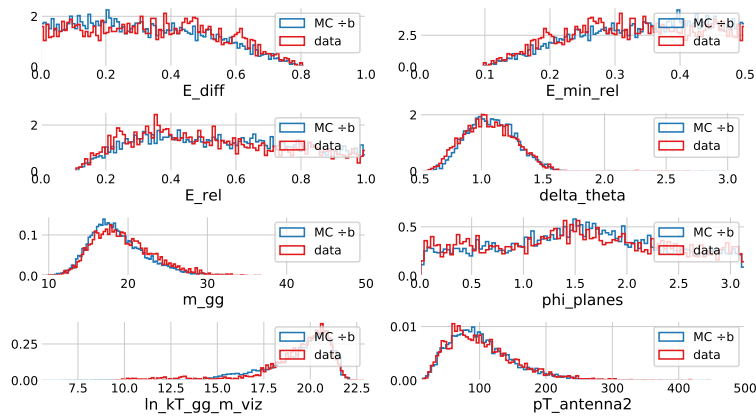


Figure 6.27: R kt CA cut region A XXX **TODO!**

B. Quarks vs. Gluons Appendix

	b	c	uds	g	non- q -matched
2	37.2 %	12.9 %	29.1 %	0.0 %	20.7 %
3	22.6 %	8.9 %	19.7 %	31.2 %	17.5 %
4	14.6 %	7.0 %	15.0 %	45.1 %	18.3 %
5	10.0 %	5.7 %	12.2 %	52.5 %	19.6 %
6	7.1 %	4.4 %	8.8 %	54.4 %	25.2 %

Table B.1: Number of different types of jets for MC and MCb written in relative numbers such that each row sum to 100 %. See also Table [6.3](#).

figures/quarks/viz_UMAP_test_0.5_input2b_njet=4_algorithm=UMAP.pdf

Figure B.1: Grid search of the two parameters `n_neighbors` and `min_dist` for the UMAP algorithm run on 4-jet events. For an explanation of these, see [section 6.2](#).

figures/quarks/viz_TSNE_MULTI_test_0.5_input2b_njet=4_algorithm=tsne_multi.pdf

Figure B.2: Visualization of the t-SNE algorithm as a function of the `perplexity` parameters for 4-jet events.

Bibliography

- [1] Advanced Topics in Machine Learning (ATML). URL <https://kurser.ku.dk/course/ndak15014u>.
- [2] Allstate Claims Severity - Fair Loss. URL <https://kaggle.com/c/allstate-claims-severity>.
- [3] Dmlc/xgboost. URL <https://github.com/dmlc/xgboost>.
- [4] HEP meets ML award | The Higgs Machine Learning Challenge. URL <https://higgsml.lal.in2p3.fr/prizes-and-award/award/>.
- [5] The Large Electron-Positron Collider | CERN. URL <https://home.cern/science/accelerators/large-electron-positron-collider>.
- [6] Scikit-hep/uproot. URL <https://github.com/scikit-hep/uproot>.
- [7] Datashader: Revealing the Structure of Genuinely Big Data. URL <https://github.com/holoviz/datashader>.
- [8] O. . Www.OIS.dk - Din genvej til ejendomsdata. URL <https://www.ois.dk/>.
- [9] Y. S. Abu-Mostafa, M. Magdon-Ismail, and H.-T. Lin. *Learning From Data*. AMLBook. ISBN 978-1-60049-006-4.
- [10] D. Albanese, S. Riccadonna, C. Donati, and P. Franceschi. A practical tool for maximal information coefficient analysis. 7. ISSN 2047-217X. doi: 10.1093/gigascience/gy032. URL <https://doi.org/10.1093/gigascience/gy032>.
- [11] E. Anderson. The Species Problem in Iris. 23(3):457–509. ISSN 00266493. doi: 10.2307/2394164. URL www.jstor.org/stable/2394164.
- [12] B. Andersson, G. Gustafson, G. Ingelman, and T. Sjöstrand. Parton fragmentation and string dynamics. 97(2):31–145. ISSN 0370-1573. doi: 10.1016/0370-1573(83)90080-7. URL <http://www.sciencedirect.com/science/article/pii/0370157383900807>.

- [13] S. R. Armstrong. A Search for the standard model Higgs boson in four jet final states at center-of-mass energies near 183-GeV with the ALEPH detector at LEP. URL <http://wwwlib.umi.com/dissertations/fullcit?p9910371>.
- [14] M. Awad and R. Khanna. Support Vector Regression. In M. Awad and R. Khanna, editors, *Efficient Learning Machines: Theories, Concepts, and Applications for Engineers and System Designers*, pages 67–80. Apress. ISBN 978-1-4302-5990-9. doi: 10.1007/978-1-4302-5990-9_4. URL https://doi.org/10.1007/978-1-4302-5990-9_4.
- [15] R. J. Barlow. *Statistics: A Guide to the Use of Statistical Methods in the Physical Sciences (Manchester Physics Series)*. WileyBlackwell, reprint edition. ISBN 0-471-92295-1. URL <http://www.amazon.co.uk/Statistics-Statistical-Physical-Sciences-Manchester/dp/0471922951%3FSubscriptionId%3D13CT5CVB80YFWJEPWS02%26tag%3Dws%26linkCode%3Dxm2%26camp%3D2025%26creative%3D165953%26creativeASIN%3D0471922951>.
- [16] J. T. Barron. A General and Adaptive Robust Loss Function. URL <http://arxiv.org/abs/1701.03077>.
- [17] W. Bartel et al. Experimental study of jets in electron-positron annihilation. 101(1):129–134. ISSN 0370-2693. doi: 10.1016/0370-2693(81)90505-0. URL <http://www.sciencedirect.com/science/article/pii/0370269381905050>.
- [18] E. Becht, C.-A. Dutertre, I. W. H. Kwok, L. G. Ng, F. Ginhoux, and E. W. Newell. Evaluation of UMAP as an alternative to t-SNE for single-cell data. page 298430, . doi: 10.1101/298430. URL <https://www.biorxiv.org/content/10.1101/298430v1>.
- [19] E. Becht, L. McInnes, J. Healy, C.-A. Dutertre, I. W. H. Kwok, L. G. Ng, F. Ginhoux, and E. W. Newell. Dimensionality reduction for visualizing single-cell data using UMAP. 37(1):38–44, . ISSN 1546-1696. doi: 10.1038/nbt.4314. URL <https://www.nature.com/articles/nbt.4314>.
- [20] J. Bergstra and Y. Bengio. Random Search for Hyperparameter Optimization. 13:281–305. ISSN 1532-4435. URL <http://dl.acm.org/citation.cfm?id=2188385.2188395>.
- [21] C. Bierlich. Rope hadronization, geometry and particle production in pp and pA Collisions. URL <https://lup.lub.lu.se/search/ws/files/18474576/thesis.pdf>.
- [22] Bolighed. Bolighed - usikkerhed i data-vurderingen. URL <https://bolighed.dk/om-bolighed/spoergsmaal-og-svar/#boligvaerdi>.

- [23] L. Breiman. Random Forests. 45(1):5–32. ISSN 1573-0565. doi: 10.1023/A:1010933404324. URL <https://doi.org/10.1023/A:1010933404324>.
- [24] E. Brochu, V. M. Cora, and N. de Freitas. A Tutorial on Bayesian Optimization of Expensive Cost Functions, with Application to Active User Modeling and Hierarchical Reinforcement Learning. URL <http://arxiv.org/abs/1012.2599>.
- [25] R. Brun and F. Rademakers. ROOT — An object oriented data analysis framework. 389(1):81–86. ISSN 0168-9002. doi: 10.1016/S0168-9002(97)00048-X. URL <http://www.sciencedirect.com/science/article/pii/S016890029700048X>.
- [26] A. Buckley, J. Butterworth, S. Gieseke, D. Grellscheid, S. Hoche, H. Hoeth, F. Krauss, L. Lonnblad, E. Nurse, P. Richardson, S. Schumann, M. H. Seymour, T. Sjostrand, P. Skands, and B. Webber. General-purpose event generators for LHC physics. 504(5):145–233. ISSN 03701573. doi: 10.1016/j.physrep.2011.03.005. URL <http://arxiv.org/abs/1101.2599>.
- [27] C. Burgard. Standard model of physics | TikZ example. URL <http://www.texample.net/tikz/examples/model-physics/>.
- [28] D. Buskulic et al. An investigation of B_d and B_s oscillation. 322(4):441–458. ISSN 0370-2693. doi: 10.1016/0370-2693(94)91177-0. URL <http://www.sciencedirect.com/science/article/pii/0370269394911770>.
- [29] T. Chen and C. Guestrin. XGBoost: A Scalable Tree Boosting System. pages 785–794. doi: 10.1145/2939672.2939785. URL <http://arxiv.org/abs/1603.02754>.
- [30] T. A. Collaboration. Observation of a new particle in the search for the Standard Model Higgs boson with the ATLAS detector at the LHC. 716(1):1–29. ISSN 03702693. doi: 10.1016/j.physletb.2012.08.020. URL <http://arxiv.org/abs/1207.7214>.
- [31] A. Diaz-Papkovich, L. Anderson-Trocmé, C. Ben-Eghan, and S. Gravel. UMAP reveals cryptic population structure and phenotype heterogeneity in large genomic cohorts. 15(11). ISSN 1553-7390. doi: 10.1371/journal.pgen.1008432. URL <https://www.ncbi.nlm.nih.gov/pmc/articles/PMC6853336/>.
- [32] S. D. DST. Price Index (EJ14) - Statistics Denmark. URL <https://www.dst.dk/en/Statistik/emner/priser-og-forbrug/ejendomme>.
- [33] D. et al. Buskulic. A precise measurement of hadrons. 313(3): 535–548. ISSN 0370-2693. doi: 10.1016/0370-2693(93)90028-G. URL <http://www.sciencedirect.com/science/article/pii/037026939390028G>.

- [34] R. A. Fisher. The Use of Multiple Measurements in Taxonomic Problems. 7(2):179–188. ISSN 2050-1439. doi: 10.1111/j.1469-1809.1936.tb02137.x. URL <https://onlinelibrary.wiley.com/doi/abs/10.1111/j.1469-1809.1936.tb02137.x>.
- [35] Y. Freund and R. E. Schapire. A decision-theoretic generalization of on-line learning and an application to boosting. In P. Vitányi, editor, *Computational Learning Theory*, pages 23–37. Springer Berlin Heidelberg. ISBN 978-3-540-49195-8. Adaboost.
- [36] S. L. Glashow. Partial-symmetries of weak interactions. 22(4): 579–588. ISSN 0029-5582. doi: 10.1016/0029-5582(61)90469-2. URL <http://www.sciencedirect.com/science/article/pii/0029558261904692>.
- [37] A. E. Harvey and S. Peters. Estimation Procedures for Structural Time Series Models. doi: 10.1002/for.3980090203.
- [38] T. Hastie and R. Tibshirani. Generalized Additive Models: Some Applications. 82(398):371–386. ISSN 01621459. doi: 10.2307/2289439. URL www.jstor.org/stable/2289439.
- [39] T. Hastie, R. Tibshirani, and J. Friedman. *The Elements of Statistical Learning: Data Mining, Inference, and Prediction, Second Edition*. Springer Series in Statistics. Springer-Verlag, 2 edition. ISBN 978-0-387-84857-0. URL [//www.springer.com/la/book/9780387848570](http://www.springer.com/la/book/9780387848570).
- [40] P. Huber and E. Ronchetti. *Robust Statistics*. Wiley Series in Probability and Statistics. Wiley. ISBN 978-1-118-21033-8. URL https://books.google.dk/books?id=j10hquR_j88C.
- [41] S. Hviid, Juul. Working Paper: A regional model of the Danish housing market. URL <http://www.nationalbanken.dk/en/publications/Pages/2017/11/Working-Paper-A-regional-model-of-the-Danish-housing-market.aspx>.
- [42] F. James and M. Roos. Minuit – a system for function minimization and analysis of the parameter errors and correlations. 10:343–367. doi: 10.1016/0010-4655(75)90039-9.
- [43] G. Ke, Q. Meng, T. Finley, T. Wang, W. Chen, W. Ma, Q. Ye, and T.-Y. Liu. LightGBM: A Highly Efficient Gradient Boosting Decision Tree. In I. Guyon, U. V. Luxburg, S. Bengio, H. Wallach, R. Fergus, S. Vishwanathan, and R. Garnett, editors, *Advances in Neural Information Processing Systems 30*, pages 3146–3154. Curran Associates, Inc. URL <http://papers.nips.cc/paper/6907-lightgbm-a-highly-efficient-gradient-boosting-decision-tree.pdf>.

- [44] C. Leys, C. Ley, O. Klein, P. Bernard, and L. Licata. Detecting outliers: Do not use standard deviation around the mean, use absolute deviation around the median. 49(4): 764–766. ISSN 0022-1031. doi: 10.1016/j.jesp.2013.03.013. URL <http://www.sciencedirect.com/science/article/pii/S0022103113000668>.
- [45] S. M. Lundberg and S.-I. Lee. A unified approach to interpreting model predictions. In *Proceedings of the 31st International Conference on Neural Information Processing Systems, NIPS'17*, pages 4768–4777. Curran Associates Inc. ISBN 978-1-5108-6096-4. URL <http://dl.acm.org/citation.cfm?id=3295222.3295230>.
- [46] S. M. Lundberg, G. G. Erion, and S.-I. Lee. Consistent Individualized Feature Attribution for Tree Ensembles - SHAP. . URL <http://arxiv.org/abs/1802.03888>.
- [47] S. M. Lundberg, G. G. Erion, and S.-I. Lee. Consistent Individualized Feature Attribution for Tree Ensembles. . URL <http://arxiv.org/abs/1802.03888>.
- [48] L. McInnes and J. Healy. UMAP: Uniform Manifold Approximation and Projection for Dimension Reduction. URL <http://arxiv.org/abs/1802.03426>.
- [49] I. Mulalic, H. Rasmussen, J. Rouwendal, and H. H. Woltmann. The Financial Crisis and Diverging House Prices: Evidence from the Copenhagen Metropolitan Area. ISSN 1556-5068. doi: 10.2139/ssrn.3041272. URL <https://www.ssrn.com/abstract=3041272>.
- [50] Particle Data Group et al. Review of Particle Physics. 98(3):030001. doi: 10.1103/PhysRevD.98.030001. URL <https://link.aps.org/doi/10.1103/PhysRevD.98.030001>.
- [51] F. Pedregosa, G. Varoquaux, A. Gramfort, V. Michel, B. Thirion, O. Grisel, M. Blondel, P. Prettenhofer, R. Weiss, V. Dubourg, J. Vanderplas, A. Passos, D. Cournapeau, M. Brucher, M. Perrot, and E. Duchesnay. Scikit-learn: Machine learning in Python. 12:2825–2830.
- [52] E. Polley and M. van der Laan. Super Learner In Prediction. URL <https://biostats.bepress.com/ucbbiostat/paper266>.
- [53] J. Proriol, J. Jousset, C. Guicheney, A. Falvard, P. Henrard, D. Pallin, P. Perret, and B. Brandl. TAGGING B QUARK EVENTS IN ALEPH WITH NEURAL NETWORKS (comparison of different methods : Neural Networks and Discriminant Analysis). page 27.
- [54] A. Purcell. Go on a particle quest at the first CERN webfest. URL <https://cds.cern.ch/record/1473657>.

- [55] D. N. Reshef, Y. A. Reshef, H. K. Finucane, S. R. Grossman, G. McVean, P. J. Turnbaugh, E. S. Lander, M. Mitzenmacher, and P. C. Sabeti. Detecting Novel Associations in Large Data Sets. 334(6062):1518–1524. ISSN 0036-8075, 1095-9203. doi: 10.1126/science.1205438. URL <http://science.sciencemag.org/content/334/6062/1518>.
- [56] P. J. Rousseeuw and C. Croux. Alternatives to the Median Absolute Deviation. 88(424):1273–1283. ISSN 0162-1459. doi: 10.1080/01621459.1993.10476408. URL <https://www.tandfonline.com/doi/abs/10.1080/01621459.1993.10476408>.
- [57] A. Salam. Weak and electromagnetic interactions. In *Selected Papers of Abdus Salam*, volume Volume 5 of *World Scientific Series in 20th Century Physics*, pages 244–254. WORLD SCIENTIFIC. ISBN 978-981-02-1662-7. doi: 10.1142/9789812795915_0034. URL https://www.worldscientific.com/doi/abs/10.1142/9789812795915_0034.
- [58] L. Scodellaro. B tagging in ATLAS and CMS. URL <http://arxiv.org/abs/1709.01290>.
- [59] L. Shapley. A value for n-person games. In *The Shapley Value*, volume 28 of *Annals of Math Studies*, pages 307–317. doi: 10.1017/CBO9780511528446.003.
- [60] T. Sjöstrand, S. Ask, J. R. Christiansen, R. Corke, N. Desai, P. Ilten, S. Mrenna, S. Prestel, C. O. Rasmussen, and P. Z. Skands. An Introduction to PYTHIA 8.2. 191:159–177. ISSN 00104655. doi: 10.1016/j.cpc.2015.01.024. URL <http://arxiv.org/abs/1410.3012>.
- [61] S. J. Taylor and B. Letham. Forecasting at scale. doi: 10.7287/peerj.preprints.3190v2. URL <https://peerj.com/preprints/3190>.
- [62] i. team. Iminuit – A python interface to minuit. URL <https://github.com/scikit-hep/minuit>.
- [63] R. Tibshirani. Regression Shrinkage and Selection via the Lasso. 58(1):267–288. ISSN 0035-9246. URL www.jstor.org/stable/2346178.
- [64] A. Tikhonov. *On the Stability of Inverse Problems*, volume vol. 39 of *Doklady Akademii Nauk SSSR*.
- [65] S. Toghi Eshghi, A. Au-Yeung, C. Takahashi, C. R. Bolen, M. N. Nyachienga, S. P. Lear, C. Green, W. R. Mathews, and W. E. O’Gorman. Quantitative Comparison of Conventional and t-SNE-guided Gating Analyses. 10. ISSN 1664-3224. doi: 10.3389/fimmu.2019.01194. URL <https://www.frontiersin.org/articles/10.3389/fimmu.2019.01194/full>.

- [66] d. L. M. J. van, E. C. Polley, and A. E. Hubbard. Super Learner. 6(1). ISSN 1544-6115. doi: 10.2202/1544-6115.1309. URL <https://www.degruyter.com/view/j/sagmb.2007.6.issue-1/sagmb.2007.6.1.1309/sagmb.2007.6.1.1309.xml>.
- [67] L. van der Maaten and G. Hinton. Visualizing Data using t-SNE. 9:2579–2605. ISSN 1533-7928. URL <http://www.jmlr.org/papers/v9/vandermaaten08a.html>.
- [68] F. van Veen. The Neural Network Zoo. URL <http://www.asimovinstitute.org/neural-network-zoo/>.
- [69] V. Vapnik. Principles of Risk Minimization for Learning Theory. In *Proceedings of the 4th International Conference on Neural Information Processing Systems, NIPS'91*, pages 831–838. Morgan Kaufmann Publishers Inc. ISBN 978-1-55860-222-9. URL <http://dl.acm.org/citation.cfm?id=2986916.2987018>.
- [70] P. Virtanen, R. Gommers, T. E. Oliphant, M. Haberland, T. Reddy, D. Cournapeau, E. Burovski, P. Peterson, W. Weckesser, J. Bright, S. J. van der Walt, M. Brett, J. Wilson, K. Jarrod Millman, N. Mayorov, A. R. J. Nelson, E. Jones, R. Kern, E. Larson, C. J. Carey, I. Polat, Y. Feng, E. W. Moore, J. VanderPlas, D. Laxalde, J. Perktold, R. Cimrman, I. Henriksen, E. A. Quintero, C. R. Harris, A. M. Archibald, A. H. Ribeiro, F. Pedregosa, P. van Mulbregt, and S. . . Contributors. SciPy 1.0—Fundamental Algorithms for Scientific Computing in Python. page arXiv:1907.10121. URL <https://ui.adsabs.harvard.edu/abs/2019arXiv190710121V/abstract>.
- [71] I. Wallach and R. Lilien. The protein–small-molecule database, a non-redundant structural resource for the analysis of protein-ligand binding. 25(5):615–620. ISSN 1367-4803. doi: 10.1093/bioinformatics/btp035. URL <https://academic.oup.com/bioinformatics/article/25/5/615/183421>.
- [72] S. Weinberg. A Model of Leptons. 19(21):1264–1266. doi: 10.1103/PhysRevLett.19.1264. URL <https://link.aps.org/doi/10.1103/PhysRevLett.19.1264>.
- [73] H. Wickham. Tidy data. 59(10):1–23. ISSN 1548-7660. doi: 10.18637/jss.v059.i10. URL <https://www.jstatsoft.org/v059/i10>.

Index

license, [ii](#)